Non-specific interactions govern cytosolic diffusion of nano-sized objects in mammalian cells

Fred Etoc[1,§], Elie Balloul[1,†], Chiara Vicario[1,†,§], Davide Normanno[1,2,*], Domenik Liße[3], Assa Sittner[4], Jacob Piehler[3], Maxime Dahan[1,*], Mathieu Coppey[1,*]

[1] Laboratoire Physico-Chimie, Institut Curie, CNRS UMR168, PSL Research University, Université Pierre et Marie Curie-Paris 6. 11 rue Pierre et Marie Curie, 75248 Paris - Cedex 05, France

[2] Centre de Recherche en Cancérologie de Marseille, CNRS UMR7258, Inserm U1068, Aix-Marseille Université UM105, Institut Paoli-Calmettes. 27 boulevard Leï Roure, 13273 Marseilles - Cedex 09, France

[3] Division of Biophysics, Department of Biology, Osnabrück University. Barbarastraße 11, 49076 Osnabrück, Germany

[4] Department of Infectious Diseases, Israel Institute for Biological Research. POB 19, 7410001 Ness Ziona, Israel

[†] Equally contributed to this work

[§] current address:
Center for Studies in Physics and Biology, The Rockefeller University. 1230 York Avenue, New York, NY 10065, USA (F.E.). Centre for Genomic Regulation, The Barcelona Institute of Science and Technology. Carrer del Dr. Aiguader 88, 08003 Barcelona, Spain (C.V.)

[*] Correspondence should be addressed to D.N. (davide.normanno@inserm.fr), M.D. (maxime.dahan@curie.fr), and M.C. (mathieu.coppey@curie.fr)

Supplementary Video Legends

Supplementary Video 1
Representative video of 25nm Rho-NPs diffusing in a HeLa cell after pinocytic loading. Three unburst vesicles can be seen at the top of the images: two very, close together, on the left and one, very bright, in the middle. These unburst vesicles are much larger than individual NPs and are basically immobile. Images were acquired every 10 ms, the video is encoded at 30 frames per second (fps). Scale bar represents 10 μm.

Supplementary Video 2
Representative videos of 25nm Rho-NPs diffusing in HeLa cells after pinocytic loading. Top row: crops of the field of view showing unburst vesicles. NPs encapsulated within these intact vesicles move very fast and cannot be tracked individually. Bottom row: examples of typical regions of interest chosen for NPs single-particle tracking analysis and selected in a way such that unburst vesicles were systematically excluded. The marked difference in the behaviour of free versus encapsulated NPs ensures a reliable discrimination between the two cases. Images were acquired every 10 ms, the video is encoded at 30 fps. Scale bars represent 1 μm.

Supplementary Video 3
Representative video of QDs (QDs-PEG-NH_2) diffusing in a HeLa cell after pinocytic loading. QDs clearly show *on-off* fluctuations (blinking) of the fluorescence signal (use Supplementary Fig. 4 as reference to more easily spot blinking particles). The blinking behaviour is a typical signature of individual emitters and indicates that QDs are mono-dispersed, confirming their escape from pinocytic vesicles and dismissing potential aggregations. Images were acquired every 30 ms, the video is encoded at 15 fps. The counter indicates the frame number. Scale bar represents 2 μm.

Supplementary Video 4
Representative video of the simultaneous diffusion of two different types of QDs, QDs-605 emitting at 605 nm (green) and QDs-PEG-NH_2 emitting at 655 nm (red), after concomitant pinocytic internalization. The images clearly illustrate that in the two HeLa cells visible in the video there is no co-localization of the two probes, on the contrary of what expected if NPs would have been still encapsulated inside unburst vesicles. Images were acquired every 30 ms, the video is encoded at 15 fps. Scale bar represents 5 μm.

Supplementary Video 5
The video shows the concurrent detection of the two types of QDs displayed in Supplementary Video 4: QDs-605 (red circles) and QDs-PEG-NH_2 (yellow circles). The images put well in evidence the absence of correlated dynamics in the mobility of the two probes, on the contrary of what expected if NPs would have been still encapsulated inside unburst vesicles. Images were acquired every 30 ms, the video is encoded at 10 fps. Scale bar represents 5 μm.

Supplementary Figure 1

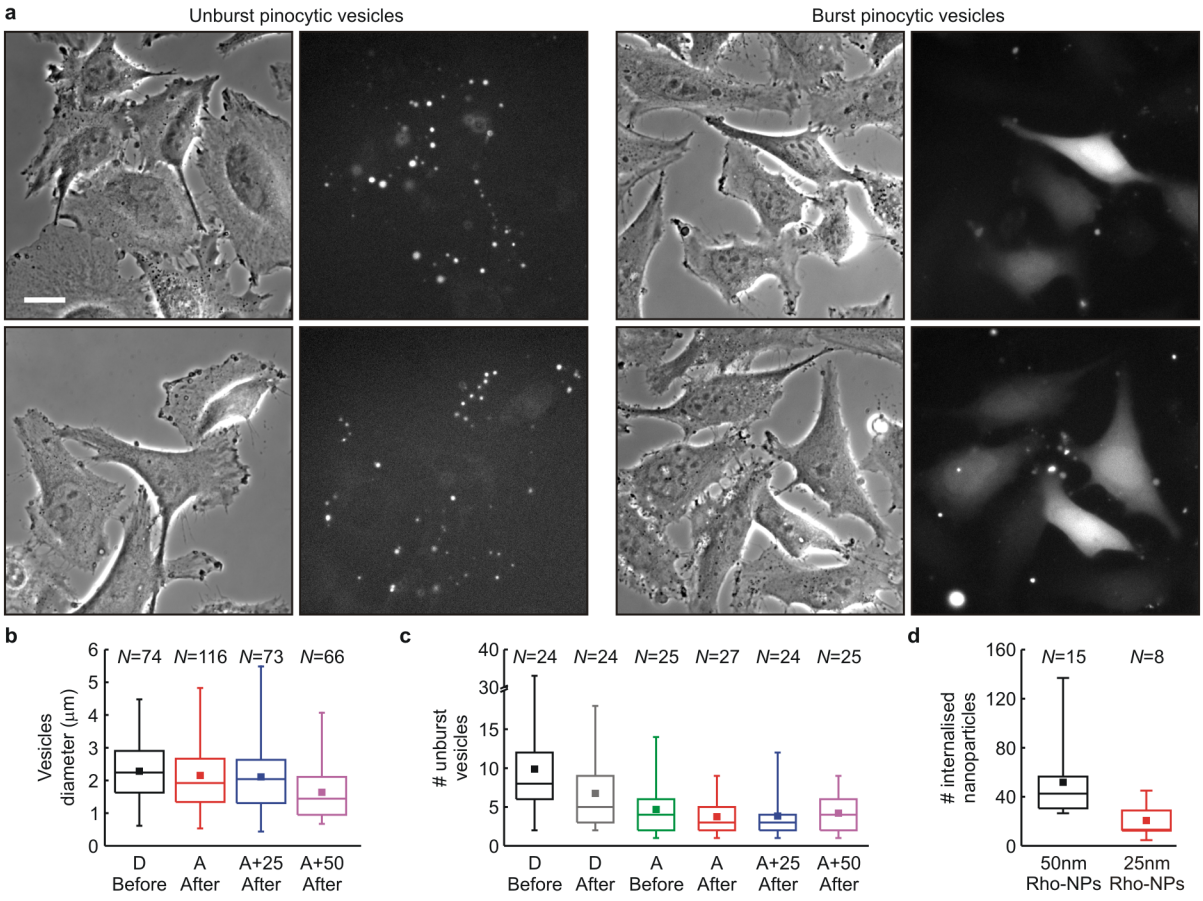

Supplementary Figure 1 | Characterization of pinocytic internalization

a) Formation and bursting of pinocytic vesicles. Left. Representative phase contrast and fluorescence images of HeLa cells containing unburst vesicles after pinocytic loading using FITC-Dextran (MW 150 kDa, concentration ~5 nM). Several pinocytic vesicles are formed in each cell: they appear as bright spots in the fluorescence images and are also visible in phase contrast. The choice to use high molecular weight Dextran was instrumental and dictated by the fact that it prevented bursting of the vesicles permitting, therefore, to quantify by fluorescence imaging the size and number of vesicles formed during pinocytosis (see Panels b and c). In fact, because of their extreme sensitivity to osmolarity, pinocytic vesicles burst even upon a gentle wash or dilution of the hypertonic medium, which prevents to reduce the extracellular fluorescence background and, thus, to image intact vesicles when filled with NPs. **Right.** Representative phase contrast and fluorescence images of HeLa cells after pinocytic loading of Atto488 (MW ~1 kDa, concentration ~70 µM) used to quantify the number of vesicles remaining intact after osmotic shock (see Panel c). Of note, the presence in the field of view of unstained cells confirms that Atto488 was internalized via pinocytosis and not via passive diffusion. Each experiment has been repeated twice. Scale bar represents 20 µm.

b) Quantification of pinocytic vesicles size. Box plots of pinocytic vesicles size quantified from fluorescence images after intensity thresholding. The size of intact vesicles was measured in the case of two different loading procedures: 10 min of *Influx* treatment in the presence of FITC-Dextran (black, "D Before"), and 10 min of *Influx* treatment in the presence of Atto488 (red, "A After") plus 25 nm (blue, "A+25 After") or 50 nm (magenta, "A+50 After") Rho-NPs followed by 2 min of hypotonic medium incubation. In all cases, vesicles ranged between about 1 and 4 μm (with a mean size of ~2 μm), thus, well above the point-spread-function of our imaging systems (~300 nm), which ensures that they can be easily distinguished from diffraction-limited NPs. Boxes indicate 25 to 75% of the underlying distribution, central lines represent median values, solid squares denote mean values, vertical bars cover the interval from 1 to 99% of the distribution. *N* represents the number of vesicles analysed.

c) Quantification of unburst vesicles number. Box plots of the number of intact vesicles per cell in the case of two different loading procedures: 10 min of *Influx* treatment in the presence of FITC-Dextran (black, "D Before", showing an average of 8 vesicles formed per cell) or of Atto488 (green, "A Before"), and 10 min of *Influx* treatment in the presence of FITC-Dextran (grey, "D After"), Atto488 (red, "A After") plus 25 nm (blue, "A+25 After") or 50 nm (magenta, "A+50 After") Rho-NPs followed by 2 min of hypotonic medium incubation (showing on average of at most 3 unburst vesicles per cell). Boxes indicate 25 to 75% of the underlying distribution, central lines represent median values, solid squares denote mean values, vertical bars cover the interval from 1 to 99% of the distribution. *N* represents the number of cells analysed.

d) Quantification of the number of released NPs per cell. Box plots of the number of internalized nanoparticles into individual HeLa cells after 10 min of *Influx* treatment followed by 2 min of hypotonic medium incubation. We found 52 ± 32 NPs per cell (mean ± SEM) in the case of 50nm Rho-NPs (black) and 21 ± 13 for 25nm Rho-NPs (red). Boxes indicate 25 to 75% of the underlying distribution, central lines represent median values, solid squares denote mean values, vertical bars cover the interval from 1 to 99% of the distribution. *N* represents the number of cells analysed.

Supplementary Figure 2

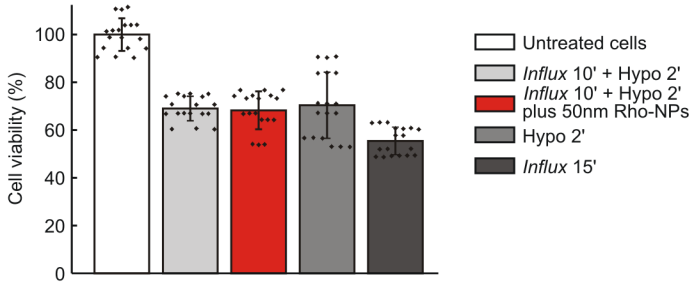

Supplementary Figure 2 | Cells are largely viable after pinocytic internalization of 50nm Rho-NPs

Cell viability was measured using a MTT-based kit (M5655, Sigma-Aldrich) following the manufacturer procedure. HeLa cells were plated on 96-well plates and were either left untreated (white) or treated with the standard pinocytosis procedure: 10 min *Influx* reagent followed by 2 min of hypotonic medium incubation. In the latter case, about 70% of cells survived to the protocol irrespectively of the absence (light grey) or the presence (red) of 50nm Rho-NPs, indicating no additional cellular toxicity of NPs. Incubation with only hypotonic medium for 2 min (Hypo) resulted in similar levels of cell viability (grey) while longer incubation with the *Influx* reagent (e.g., 15 min) reduced cell viability to less than 60% (dark grey). Column values represent the average cell viability resulting from 18 independent wells (black diamonds) pulled together from three different experimental replicas. Error bars are standard deviations.

Supplementary Figure 3

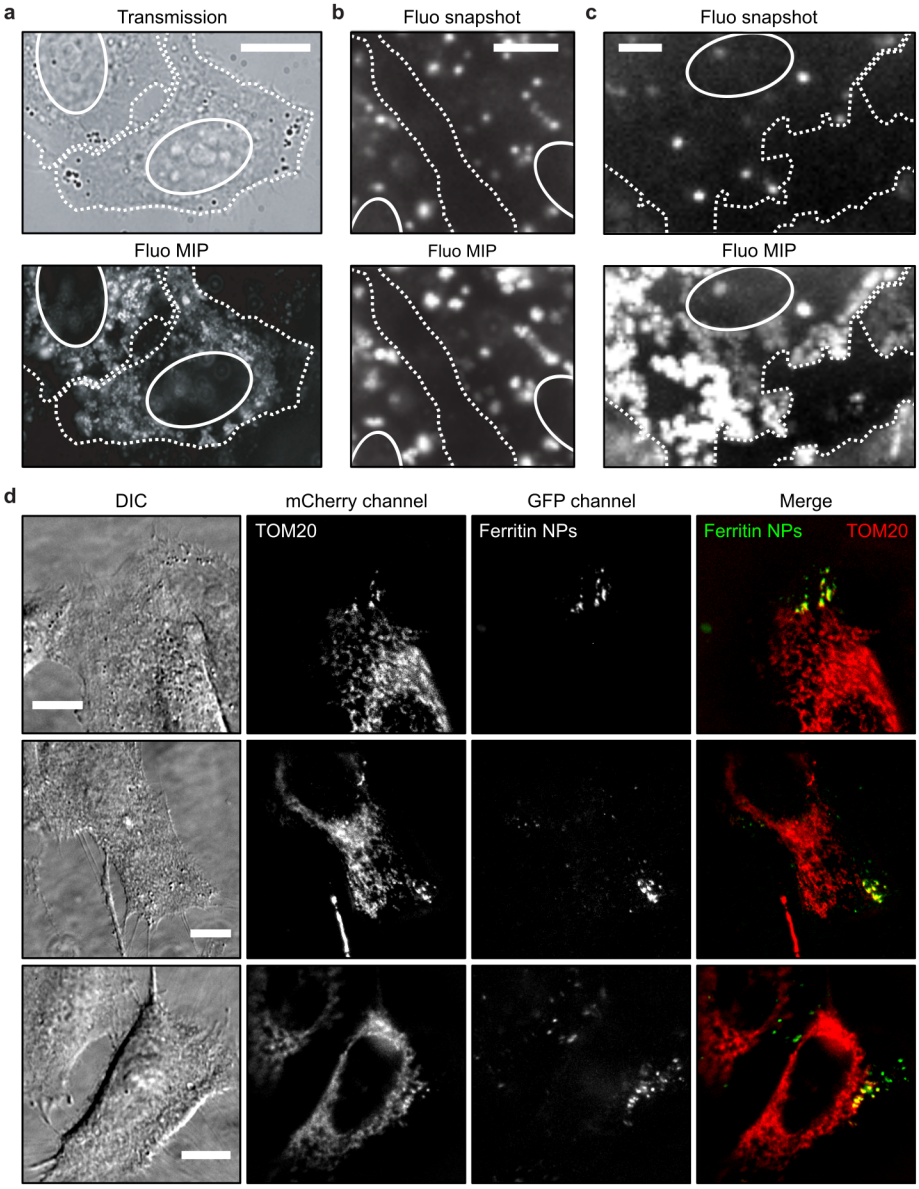

Supplementary Figure 3 | NPs internalized via pinocytosis explore the whole cytoplasm and can target intracellular components

a) QDs behaviour after pinocytic internalization. **Top.** Transmission image of two HeLa cells. **Bottom.** Maximum intensity projection (MIP) image of QDs fluorescence from a 2000 frame-long recording. QDs explore the whole cytoplasm of cells (white dotted contours), resulting in a diffuse fluorescence signal in the MIP image, but do not enter into the nuclei (white ovals), which remain dark. Internalization of QDs in living cells via pinocytosis has been achieved successfully more than 100 times. Scale bar represents 10 µm.

b) QDs intracellular exploration after passive endosomal internalization. Top. Snapshot of QDs fluorescence. **Bottom.** MIP of QDs fluorescence from a 500 frame-long recording. In this case, QDs remain trapped inside the endosomes (bright spots in both images) and do not move in the cytosol, resulting in no diffuse fluorescence signal in the MIP image. Passive endosomal internalization of QDs have been repeated twice. Scale bar represents 10 μm.
c) QDs intracellular exploration after pinocytic internalization. Top. Snapshot of QDs fluorescence. **Bottom.** MIP of QDs fluorescence from a 500 frame-long recording. Contrarily to when trapped inside endosomes (as in Panel b), after vesicles burst by osmotic shock QDs are released and explore the cytosol, resulting in a diffuse fluorescence signal in the MIP image. Pinocytic internalization of QDs have been successfully done more than 100 times. Scale bar represents 5 μm.
d) Targeting of ferritin NPs to mitochondria. Examples of HeLa cells expressing the chimeric construct GFPbinder-mCherry-TOM20 (localizing at the mitochondrial membrane) and loaded with ferritin-GFP-NPs using pinocytosis. **From left to right:** DIC images, mCherry channel, GFP channel, merge (yellow) of mCherry (red) and GFP (green) channels. Co-localization of fluorescence signals shows that ferritin-GFP-NPs could readily target mitochondria, indicating that NPs are dispersed in the cytosol and not encapsulated into pinocytic vesicles. Remarkably, targeting happened on small regions, presumably where vesicles burst, as the result of the very strong affinity (sub-nanomolar K_D) of the GFP-binder nanobody. The chimeric construct was realized fusing the GFP-binder nanobody and mCherry (used for visualization) to the cytosolic domain of TOM20. Ferritin-GFP-NPs were obtained fusing the heavy chain of ferritin to eGFP. Experiments have been repeated successfully three times. Scale bars represent 10 μm.

Supplementary Figure 4

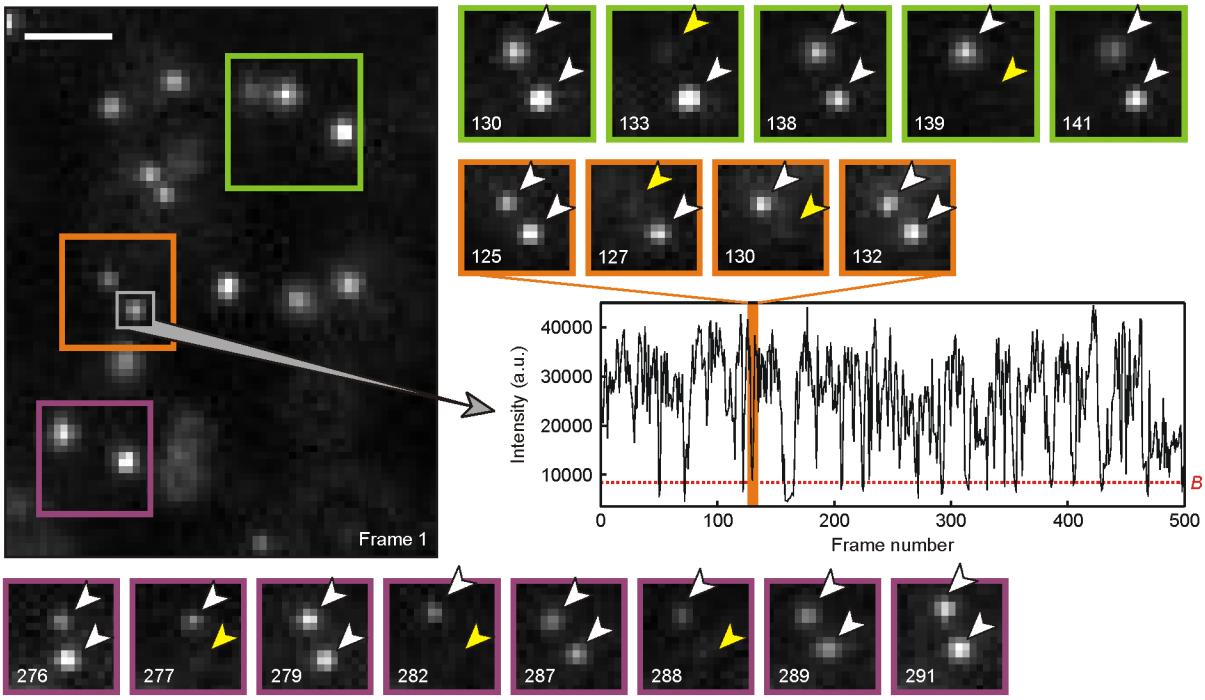

Supplementary Figure 4 | QDs show blinking after pinocytic internalization

QDs internalized in HeLa cells via pinocytosis clearly showed *on-off* blinking of the fluorescent signal, a typical signature of individual emitters. This indicates that QDs are mono-dispersed, confirming their escape from pinocytic vesicles and dismissing potential aggregations (especially important in the case of QDs that are, possibly, the probe most prone to aggregate, given their very reactive core not fully screened by the outer functional coating, as evidenced by the results presented in the main text). The large image shows the first frame of Supplementary Video 3 and small crops show sub-sequent frames of the indicated coloured boxes, both for diffusing QDs (green and purple boxes) and for immobile QDs (orange box). In the latter case, the intensity of individual QDs could be easily followed over time integrating the signal of a small region around one NP (grey box). Fluctuations are clearly visible in the corresponding intensity time-course where the red dotted line indicates the background level *B*. White arrowheads point to emitting QDs (*on* state) while yellow arrowheads to dark QDs (*off* state). Numbers at the bottom left corner of the coloured boxes indicate the frame from which the image has been extrapolated. Blinking of individual QDs was successfully observed in three independent experiments. Scale bar represents 2 μm and applies to all images.

Supplementary Figure 5

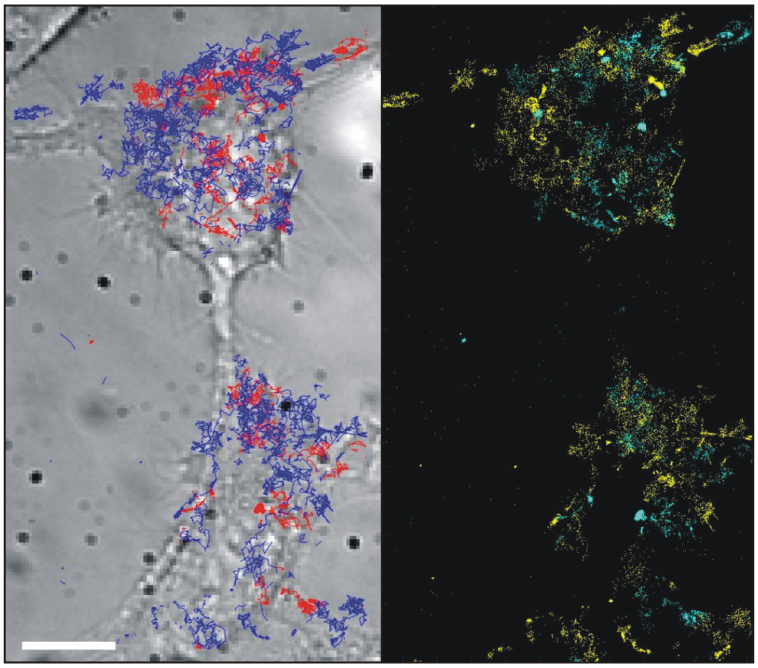

Supplementary Figure 5 | QDs of different colours do not co-localize and diffuse independently after pinocytic internalization

Left. Composite image showing two HeLa cells (grey scale) and the reconstructed trajectories of two different types of QDs simultaneously internalized via pinocytosis: QDs-605 emitting at 605 nm (red trajectories) and QDs-PEG-NH_2 emitting at 655 nm (blue trajectories). As visible, most trajectories span relatively large portions of the cells and do not show confinement within regions compatible with the size of pinocytic vesicles (which have a diameter on the order of 2 μm). **Right.** Maximal projection image showing the detections of QDs-605 (cyan dots) and of QDs-PEG-NH_2 (yellow dots). No co-localization or correlated dynamics of the two types of QDs has been observed (see also Supplementary Video 4 and 5). Moreover, given the typical numbers of vesicles formed (~8) and of NPs internalized (between 20 and 50) per cell, the average number of NPs per vesicle is 4 and the probability that all the 8 vesicles formed, on average, in a given cell would be all filled with 4 NPs of the same colour is of the order of 10^{-8}, which -despite possible- is relatively improbable and further supports the effective release of NPs from pinocytic vesicles. Dual colour experiments have been repeated twice and each time 10 cells have been imaged. Scale bar represents 5 μm.

Supplementary Figure 6

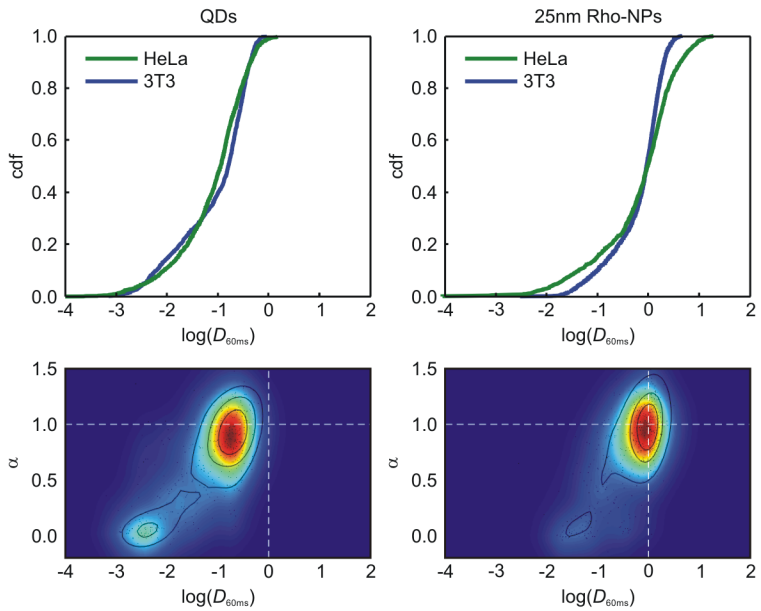

Supplementary Figure 6 | QDs and 25nm Rho-NPs have similar diffusive properties in different mammalian cell lines

Top. Cumulative distribution function of the logarithm of the instantaneous diffusivity coefficients D_{60ms} for QDs (left) and 25nm Rho-NPs (right) in human (cancerous) HeLa cells (green, N = 1696 trajectories for QDs and N = 1314 trajectories for Rho-NPs) and in murine (not cancerous) T3T fibroblasts (blue, N = 1316 trajectories for QDs and N = 2768 trajectories for Rho-NPs). No substantial quantitative differences emerged from experiments, suggesting uniformity of NPs behaviour in different mammalian cell lines. **Bottom.** Density plots in the α-D_{60ms} plane for QDs (left, N = 586 trajectories lasting more than 40 frames, out of 1316 trajectories) and 25nm Rho-NPs (right, N = 698 trajectories lasting more than 40 frames, out of 2768 trajectories) in 3T3 fibroblasts. D_{60ms} is expressed in $\mu m^2 \cdot s^{-1}$.

Supplementary Figure 7

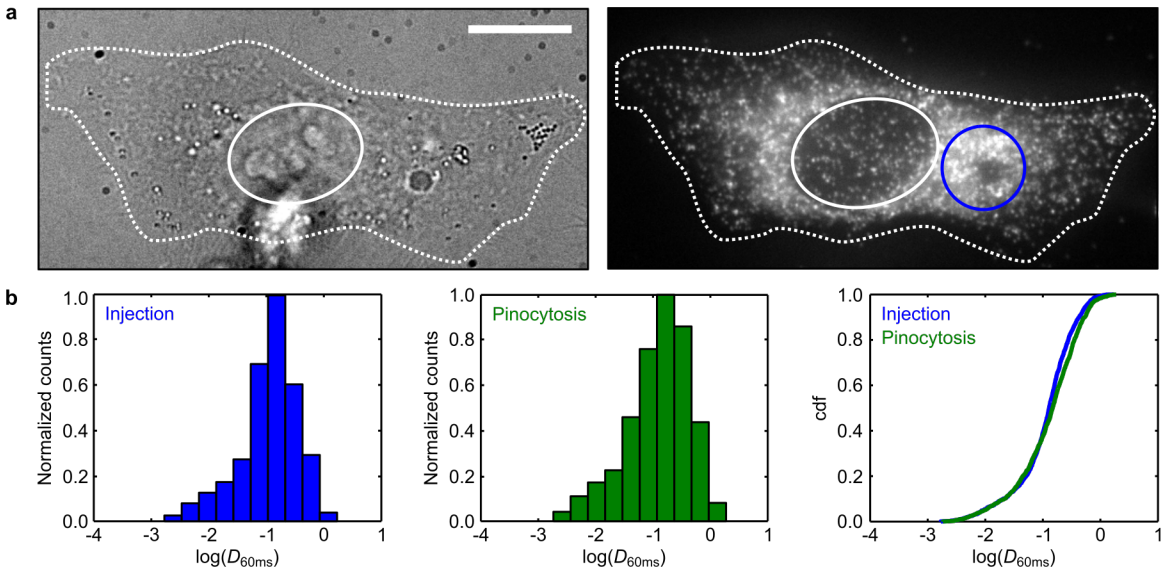

Supplementary Figure 7 | Microinjected NPs show identical diffusive properties than NPs internalized via pinocytosis

a) QDs microinjection. Left. Transmission image of a 3T3 cell (white dotted contour, white oval indicates the cell nucleus). **Right.** Corresponding fluorescence image of microinjected QDs. The microinjection locus is highlighted by the blue circle and contains a higher density of low mobility NPs. Microinjection experiments were repeated on more than 100 cells in four independent samples. Scale bar indicates 10 μm.
b) Comparison of NPs mobility for the two internalization methods. From left to right. Normalized distribution of the logarithm of D_{60ms} for QDs microinjected in HeLa cells (blue). Normalized distribution of the logarithm of D_{60ms} for QDs internalized in HeLa cells via pinocytosis (green). Cumulative distribution function of the logarithm of D_{60ms} for QDs microinjected (blue) and internalized via pinocytic loading (green) in HeLa cells. In both representations (histogram and cdf curve), N = 1547 trajectories of microinjected QDs and N = 1696 trajectories of QDs internalized via pinocytosis. D_{60ms} is expressed in $\mu m^2 \cdot s^{-1}$.

Supplementary Figure 8

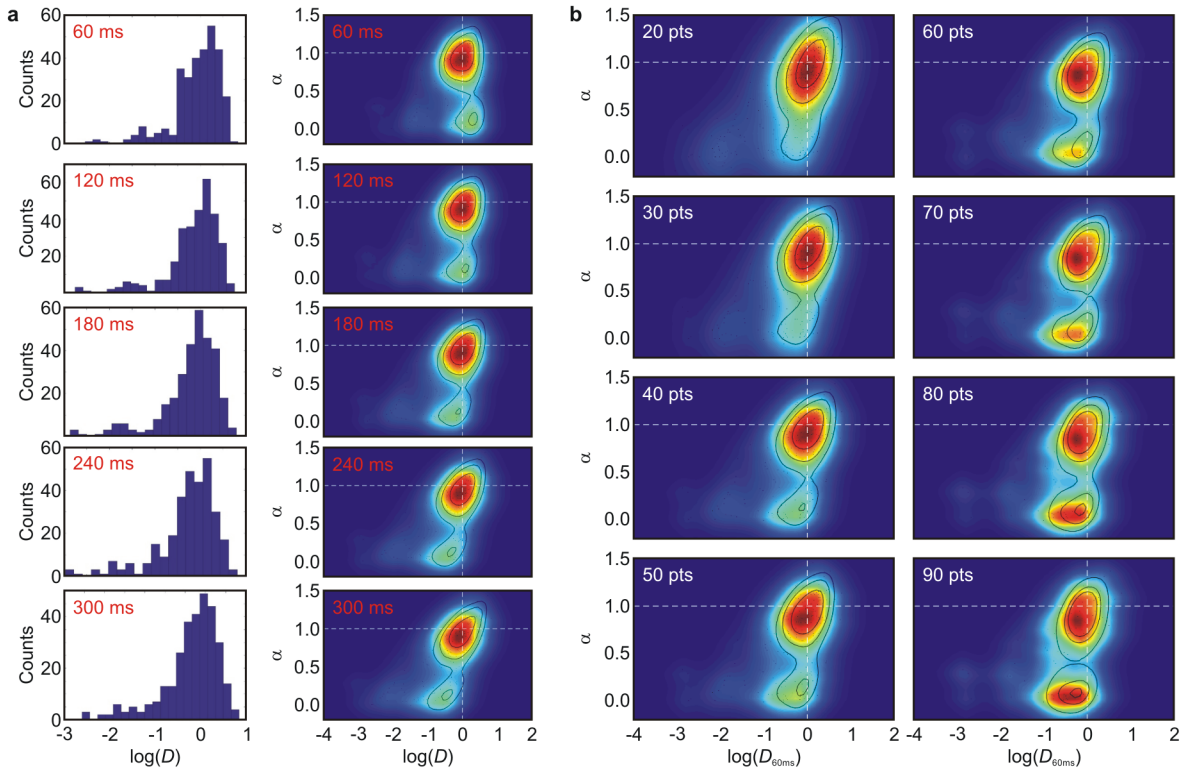

Supplementary Figure 8 | α-D_{60ms} maps are robust with respect to the parameters used for their computation

a) Dependency on the time lag considered for the calculation of the instantaneous diffusivity coefficient *D*. Distributions of the logarithm of *D* (left) and α-*D* maps (right) computed considering increasing time lags (60, 120, 180, 240, and 300 ms) for the calculation of the instantaneous diffusivity coefficient *D*.

b) Dependency on the minimal trajectory length. α-D_{60ms} maps computed considering an increasing minimal trajectory length (from 20 to 90 time points). Whereas the dependency on the time lag considered for the calculation of the instantaneous diffusivity coefficient *D* is marginal, the dependency of α-D_{60ms} maps on the minimal trajectory length is more marked. In the results presented in the main text and in Supplementary Fig. 6 and 9, we used a minimal trajectory length of 40 time points to compute the α-D_{60ms} maps. We considered that this choice represented a suitable trade-off between having trajectories long enough to limit data scattering in the maps but still short enough to avoid the strong bias towards severely sub-diffusive trajectories (which will have the tendency to remaining longer in the focal plane generating long trajectories), as highlighted by the results shown in Fig. 3a,b of the main text.

The dataset used for the analysis presented in both panels above is that relative to 25nm Rho-NPs internalized in HeLa cells via pinocytosis (same dataset used in Fig. 1b and Fig. 2b of the main text, $N = 309$ trajectories). *D* and D_{60ms} are expressed in $\mu m^2 \cdot s^{-1}$.

Supplementary Figure 9

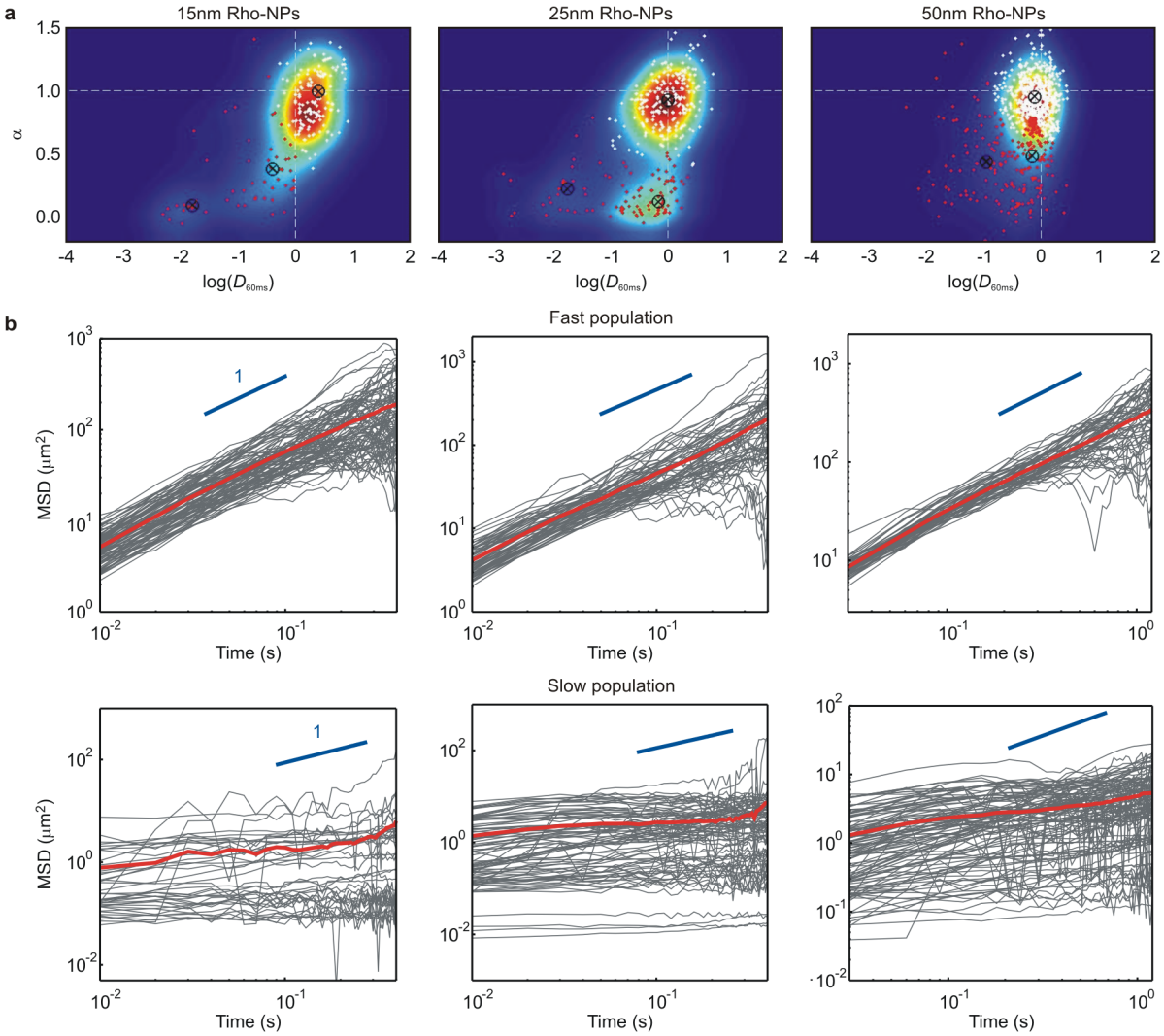

Supplementary Figure 9 | Identification and analysis of Rho-NPs subpopulations

a) Subpopulation identification via cluster analysis. To discriminate between fast and slow Rho-NPs subpopulations, we used the *k*-mean algorithm in MATLAB to cluster data points in the α-D_{60ms} plane. Two clusters failed to satisfactorily separate the two subpopulations. Thus, we used four clusters and grouped together the two clusters with largest mean D_{60ms} to select trajectories belonging to the fast population (white points in the maps), and the two clusters with the smallest mean D_{60ms} to infer trajectories belonging to the slow population (red points in the maps). Cluster centroids are indicated by black crosses. Relative fractions and mean D_{60ms} values of the two subpopulations are reported in Supplementary Table 1. 75nm Rho-NPs being mostly immobile, or very slowly diffusing, were not considered for the subpopulation analysis. The number of trajectories in the α-D_{60ms} maps is: $N = 186$ for 15nm Rho-NPs, $N = 309$ for 25nm Rho-NPs, and $N = 837$ for 50nm Rho-NPs. D_{60ms} is expressed in $\mu m^2 \cdot s^{-1}$.

b) MSD curves of fast and slow Rho-NPs subpopulations. Individual time-averaged MSDs (grey curves), in log-log scale, for the indicated Rho-NPs in HeLa cells after classification into fast (top row) and slow (bottom row) subpopulation with the cluster analysis. Blue lines have a slope of 1 (Brownian diffusion), red lines are ensemble averages. The fraction of trajectories in each of the two subpopulations is reported in Supplementary Table 1.

Supplementary Figure 10

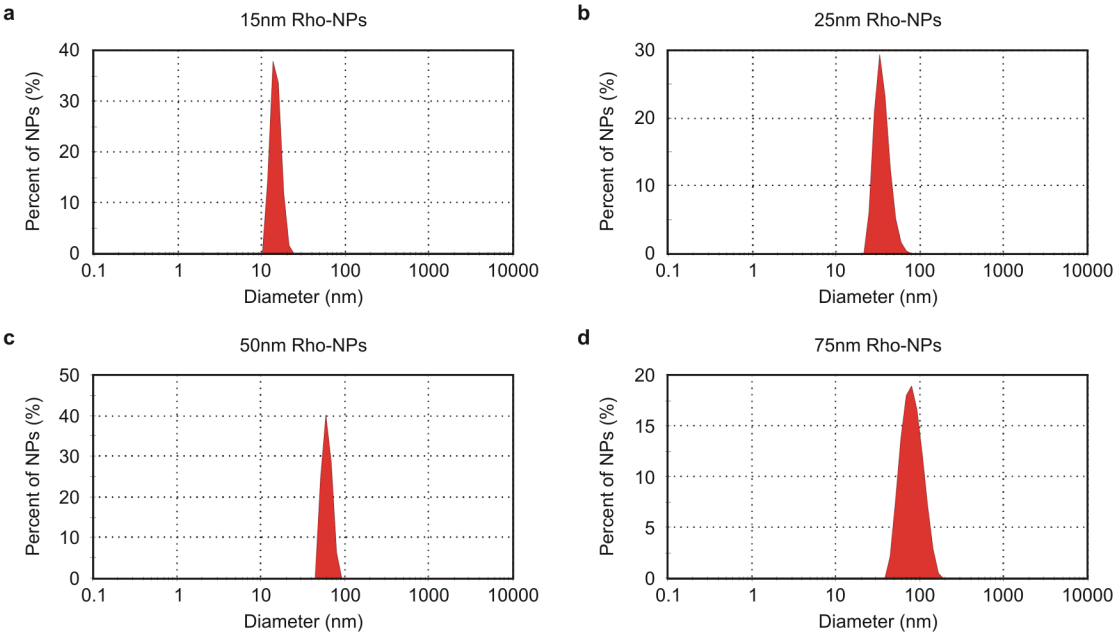

Supplementary Figure 10 | Size distribution of Rho-NPs

Distribution of Rho-NPs diameter measured by dynamic light scattering (courtesy of micromod Partikeltechnologie GmbH).
a) 15nm (plain NH_2) Rho-NPs (product no. 30-01-151, lot no. 0030930-00) have a size of (15 ± 2) nm. $N = 8 \times 10^6$ particles.
b) 25nm (streptavidin) Rho-NPs (product no. 30-19-251, lot no. 0451130-00) have a size of (35 ± 8) nm. $N = 12.1 \times 10^6$ particles.
c) 50nm (streptavidin) Rho-NPs (product no. 30-19-501, lot no. 0101230-1) have a size of (56 ± 9) nm. $N = 7.5 \times 10^6$ particles.
d) 75nm (streptavidin) Rho-NPs (product no. 30-19-751, lot no. 0211230-00) have a size of (77 ± 14) nm. $N = 27.7 \times 10^6$ particles.
Reported NPs size values are mean ± SEM.

Supplementary Figure 11

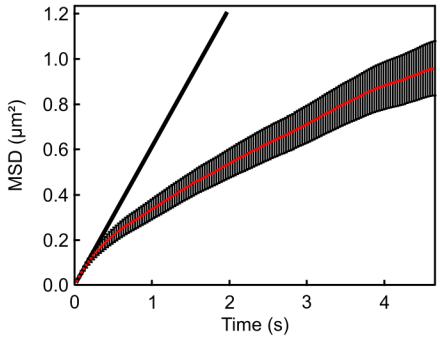

Supplementary Figure 11 | The ensemble-averaged MSD of QDs is sub-linear

The graph shows (in linear scale) the ensemble average of all individual, temporally-averaged MSDs, $\langle\langle r^2\rangle_T\rangle_E$, of QDs internalized in HeLa cells via pinocytosis (N = 1696 trajectories, same dataset than in Fig. 1c and Fig. 3a of the main text). The sub-linearity is clearly shown by the difference between the MSD curve obtained for QDs (red) and the straight line (black) corresponding to the MSD of a Brownian particle with a diffusion coefficient equal to the instantaneous diffusivity coefficient of QDs, $D_{60ms} = (0.15 \pm 0.01)\ \mu m^2 \cdot s^{-1}$. Error bars represent SEM.

Supplementary Figure 12

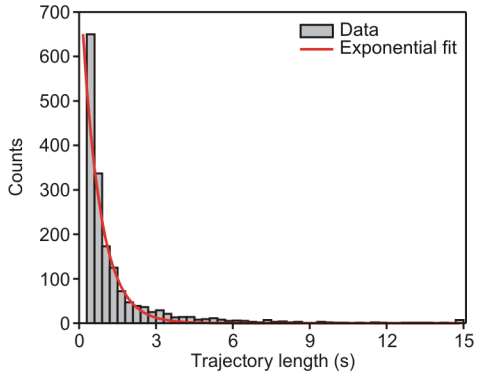

Supplementary Figure 12 | Trajectory length follows an exponential distribution

The histogram (grey columns) shows the trajectory length distribution relative to QDs internalized in HeLa cells via pinocytosis. Red line represents the best fit to data using a mono-exponential decay function ($\tau = 0.7 \pm 0.1$ s). $N = 1696$ trajectories.

Supplementary Figure 13

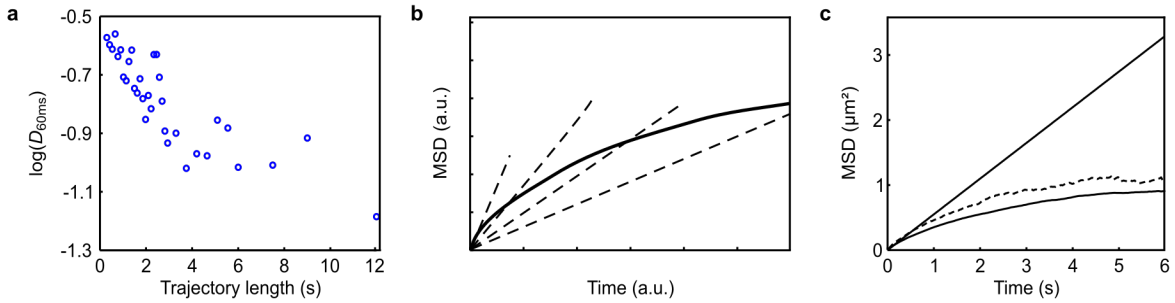

Supplementary Figure 13 | Averaging of trajectories with different lengths results in artefactual sub-diffusivity

a) Dependence of D_{60ms} on trajectory length. Scatter plot of the logarithm of the instantaneous diffusivity coefficient D_{60ms} as a function of the trajectory length for QDs internalized via pinocytosis in HeLa cells ($N = 1696$ trajectories, binned into 34 intervals of different trajectory lengths). Data clearly indicate a negative correlation between D_{60ms} and the trajectory length: the longer the trajectory the smaller the instantaneous diffusivity coefficient. As a consequence, length has a pronounced effect in trajectory analysis (as shown for 25nm Rho-NPs in Supplementary Fig. 8b) and, if not properly taken into account, it may profoundly affect the analysis of the ensemble behaviour of NPs (see Fig. 3a,b of the main text). Furthermore, at long time scales, the bias towards slow (and severely sub-diffusive) trajectories reflects into an accentuated, or even artefactual, sub-diffusive ensemble behaviour of NPs (see Panels b and c). D_{60ms} is expressed in $\mu m^2 \cdot s^{-1}$.
b) Artefactual sub-diffusivity of averaged MSDs. The graph shows four fictive linear MSDs curves (dashed lines). They represent theoretical MSDs of four Brownian particles with four different diffusion coefficients. As in experiments, rapidly diffusing particles leave quickly the observation volume, resulting in short trajectories and MSD curves extended over few time lags. Inversely, slowly diffusing particles have longer trajectories and MSD curves. Averaging of such not homogeneous, although linear, MSD curves gives rise to an artefactual sublinear ensemble MSD (solid line).
c) Ensemble averaging of Brownian trajectories -artificially generated from QDs data- shows sub-diffusion. For each recorded trajectory (of QDs in HeLa cells), we extracted two parameters: the trajectory length L and the instantaneous diffusivity coefficient D_{60ms}. From these two parameters, we build a set of linear MSD curves, each of them having duration L and slope determined by D_{60ms}. Remarkably, such an artificial set of perfectly Brownian MSDs resulted in a sub-diffusive ensemble-averaged MSD (dashed line), with approximately the same shape of the experimental one (solid line, same as red curve in Supplementary Fig. 11) and markedly deviating from Brownian diffusion (solid straight line).
Although rough, the calculations reported above (Panels b and c) highlight how sub-diffusive behaviour can emerge as an artefact inherent to the averaging over a set of purely Brownian trajectories with different length.

Supplementary Figure 14

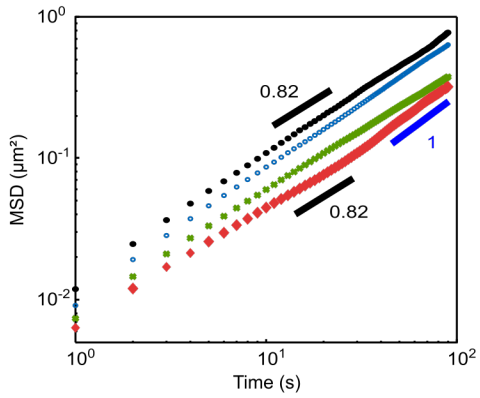

Supplementary Figure 14 | Drug treatments have minor effects on QDs diffusive behaviour

The figure shows ensemble-averaged MSD curves of QDs in log-log scale, computed considering trajectories lasting more than 90 frames, obtained in HeLa cells after different drug treatments: basal conditions -untreated cells- (black), Nocodazole (0.1 μM) treated cells (blue), Latrunculin-A (0.1 μM) treated cells (green), Brefeldin-A (5 μM) treated cells (red). Despite slight variations in diffusivity (vertical spread of the curves), all MSDs are linear (in log-log scale) and, remarkably, they all have the same slope (0.82), pointing to an intrinsic anomalous behaviour of QDs, very mildly or not affected at all by the drug treatments used. In fact, only for Brefeldin-A treatment, and only at a long timescale, we could observe a deviation of the value of the MSD slope (from 0.82 to 1). QDs were internalised in HeLa cells via pinocytosis. Basal conditions: N = 216 trajectories lasting more than 90 frames, out of 1696 trajectories. Nocodazole treated cells: N = 486 trajectories out of 2189 trajectories. Latrunculin-A treated cells: N = 312 trajectories out of 1126 trajectories. Brefeldin-A treated cells: N = 220 trajectories out of 1101 trajectories.

Supplementary Figure 15

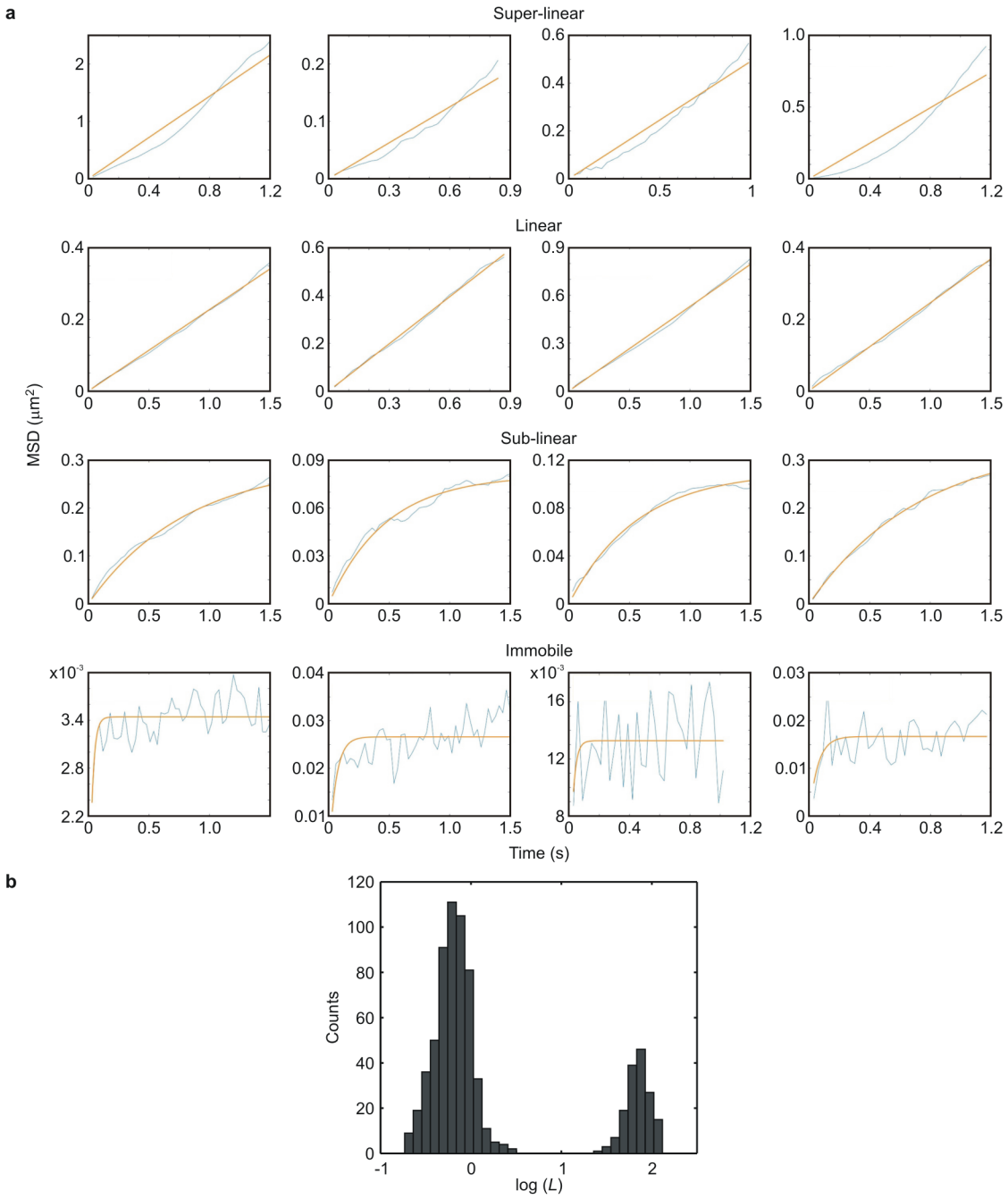

Supplementary Figure 15 | QDs mobility shows no strong evidence of confined diffusion

a) Confined diffusion fits of experimental MSD curves. Examples of time-averaged MSD curves, lasting more than 30 frames, obtained from QDs internalised in (untreated) HeLa cells via pinocytosis. MSD curves (cyan lines) have been fitted with a confined diffusion model (orange lines) using the formula: $\mathrm{MSD}(t) = L^2 \cdot (1 - \exp(-12Dt/L^2))$, where L represents

the size of the confinement box and D the diffusion coefficient. Despite MSD curves are expected to be sub-linear in the case of confined diffusion, we found also linear –and even super-linear– MSDs. Overall, four different MSD categories emerged: super-linear, linear, sub-linear, and immobile (examples of each are shown in the four rows from top to bottom, respectively).

b) Box size distribution from confined diffusion fits in basal conditions. When we globally analysed the behaviour of QDs in HeLa cells, we obtained a bimodal distribution of the logarithm of the box size L (expressed in μm, $N = 685$ trajectories), which spanned more than three orders of magnitude. The highest values of L correspond to trajectories with linear or super-linear MSDs (as in the first two rows in Panel a) that, when fitted with a confined diffusion model (even if the residuals of the fit are small), are basically fitted by straight lines, resulting in unrealistic box sizes and no physical significance of the parameter L (i.e., L larger than the cell). Conversely, the second population with smaller values of L (77% of all trajectories) corresponds to trajectories (as in the third row in Panel a) fitted with a physically plausible box size, with a mean L value of 630 nm. Nevertheless, numerical simulations showed that a similar degree of confinement (box size) is found even for unrestricted, Brownian trajectories. In fact, due to the intrinsic variability of MSD curves, even a large fraction (60%) of simulated trajectories, of particles diffusing in free space, could be fitted with a confined diffusion model, resulting into a mean box size of 850 nm (see Supplementary Table 2 and Methods for details of simulations). This value does not differ significantly from the one found experimentally and, in our view, indicates that the (putative) box size found (for QDs) is mostly a consequence of the limited temporal window of observation of QDs dynamics. Furthermore, in no case (except for completely immobile QDs, as in the last row in Panel a) we could observe a clear plateau in the MSD of individual particles, the most unambiguous signature of confined diffusion. Finally, the different drug treatments tested did not provoke substantial changes in the estimates of the mean box size values nor in the percentage of confined trajectories while, contrarily to plausible expectations, they led to reduced box sizes and to increased percentages of confined trajectories (see Supplementary Table 2). We conclude that, overall, there is no strong evidence of confined diffusion for QDs.

Supplementary Figure 16

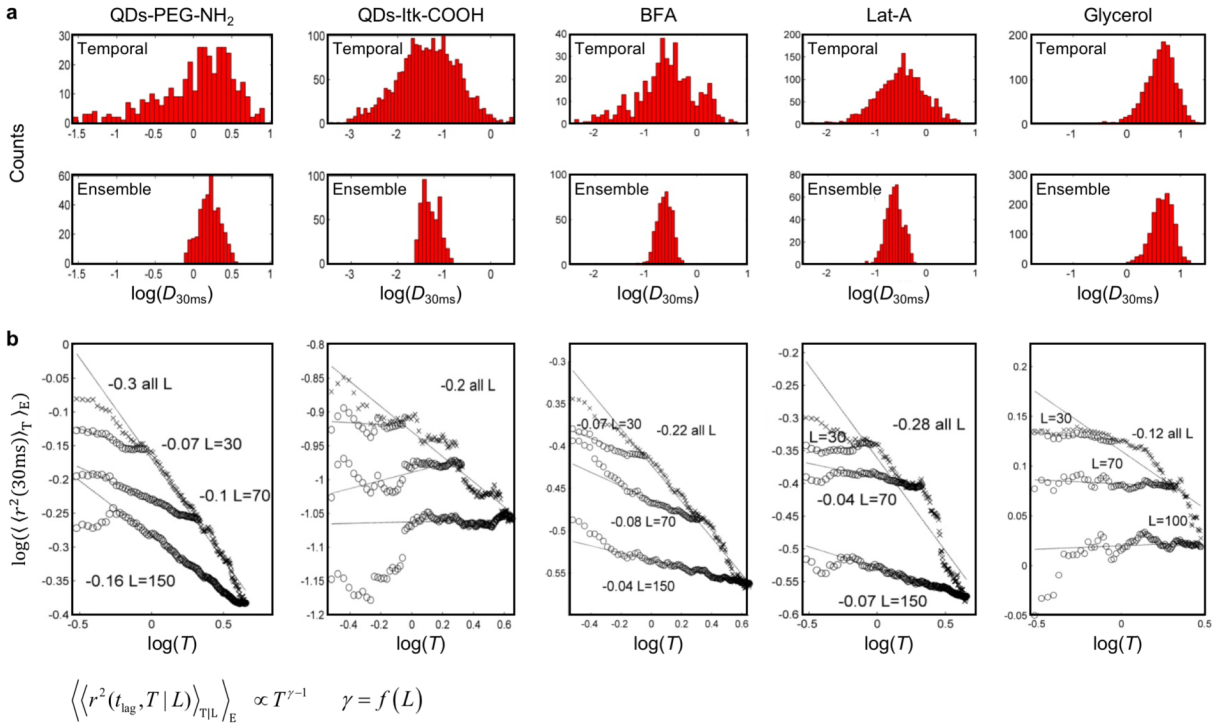

Supplementary Figure 16 | QDs trajectories show ergodicity breaking and aging

a) Ergodicity breaking. Temporal (top) versus ensemble (bottom) average distributions of the instantaneous diffusivity coefficients (calculated at 30 ms) for different probes (QDs-PEG-NH_2 and QDs-Itk-COOH) in basal conditions (untreated cells), and for QDs-PEG-NH_2 in cells treated with Brefeldin-A (BFA) or Latrunculin-A (Lat-A) or dispersed in glycerol (80% v/v in water). Ergodicity breaking is shown by the different broadness of the temporal and ensemble distributions observed in all cases but for glycerol. Experiments, except for glycerol were performed in HeLa cells and QDs internalized via pinocytosis. D_{30ms} is expressed in $\mu m^2 \cdot s^{-1}$.
b) Aging. Ensemble average of time-averaged mean square displacements (calculated using the formula reported at the bottom and expressed in μm^2) for a lag time of 30 ms as a function of the truncation time T applied to the trajectories, for the above-mentioned probes and conditions. For QD-PEG-NH_2 in basal conditions, as well as after Latrunculin-A and Brefeldin-A treatments, we observed aging in trajectories, namely a power law dependency on the truncation time T. As indicated in the graphs, the exponent of the power law depends on the length L of the trajectories considered in the analysis. For "naked" QDs (QD-Itk-COOH), we did not observe aging, probably because of the extremely long binding times and the consequent low number of moving particles. Remarkably, as expected, QDs diffusing in glycerol did not show any sign of aging, on top of no sign of ergodicity breaking.
In both panels, the number N of trajectories included in the analysis is equal to 1696 for QDs-PEG-NH_2 in untreated cells, 915 for QDs-Itk-COOH in untreated cells, 1101 for QDs-PEG-NH_2 in Brefeldin-A treated cells, 1126 for QDs-PEG-NH_2 in Latrunculin-A treated cells, and 5118 for QDs-PEG-NH_2 in 80% (v/v) glycerol.

Supplementary Figure 17

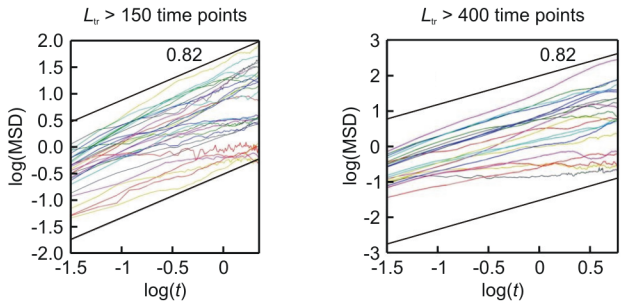

Supplementary Figure 17 | Time-averaged MSD curves of QDs show sub-diffusive behaviour

The figure shows several different examples of individual time-averaged MSD curves, in log-log scale, for QDs trajectory with length (L_{tr}) lasting more 150 (left) and 400 (right) time points. Straight black lines represent the expected MSD for anomalous diffusion with an exponent α equal to 0.82. QDs (QDs-PEG-NH_2) were internalised in (untreated) HeLa cells via pinocytosis. Experiments have been repeated three times with similar results. MSD is expressed in μm^2 and t in seconds.

Supplementary Table 1

Rho-NPs diameter	Slow population			Fast population			η_{cyto}/η_{H_2O}
	Fraction	D_{60ms} ($\mu m^2 \cdot s^{-1}$)	SEM ($\mu m^2 \cdot s^{-1}$)	Fraction	D_{60ms} ($\mu m^2 \cdot s^{-1}$)	SEM ($\mu m^2 \cdot s^{-1}$)	
15 nm	0.30	0.33	0.04	0.70	2.50	0.14	13.6
25 nm	0.33	0.51	0.05	0.67	1.34	0.07	15.2
50 nm	0.29	0.54	0.03	0.71	0.94	0.02	10.9

Supplementary Table 1 | Mobility of 15nm, 25nm, and 50nm Rho-NPs

The Table reports the mobility parameters of the fast and slow population of Rho-NPs in HeLa cells obtained using the *k*-mean algorithm for subpopulation identification and separation (see Supplementary Fig. 9a and Methods for details).
Fraction indicates the subpopulation abundance, D_{60ms} the mean diffusivity value and SEM the associated standard error of the mean.
η_{cyto} was calculated using the Stokes-Einstein equation: $D_{60ms} = k_B T / 6\pi\eta_{cyto}R$, where k_B is the Boltzmann constant, R the radius of the NPs, and considering the D_{60ms} value relative to the fast population of NPs. In the calculation, the dynamic viscosity of water (η_{H_2O}) at 37°C has been assumed to be equal to 6.9×10^{-4} N · s · m^{-2}.
The total number of trajectories considered in the analysis is N = 186 for 15nm Rho-NPs, N = 309 for 25nm Rho-NPs, and N = 837 for 50nm Rho-NPs.

Supplementary Table 2

	Basal conditions	Lat-A (100 nM)	Nocodazole (100 nM)	BFA (5 µM)	Simulated Brownian
Percentage of confined trajectories	77%	83%	75%	86%	60%
Mean box size	630 nm	500 nm	600 nm	478 nm	830 nm

Supplementary Table 2 | Effects of drug treatments on QDs confinement

The percentage of confined trajectories has been estimated from the relative amplitude of the two peaks in the bimodal distribution of the confinement box size (see Supplementary Fig. 15b). Mean box size represents the mean value of the peak with the smaller (and physically plausible) box size dimension (left peak in Supplementary Fig. 15b).
The results reported in the Table refer to QDs (QDs-PEG-NH_2) internalized in HeLa cells via pinocytosis in basal condition (N = 1696 trajectories) and after different drug treatments (N = 1126 trajectories for Lat-A; N = 2189 trajectories for Nocodazole; and N = 1101 trajectories for BFA), as well as for simulated Brownian trajectories (N = 4000 simulated trajectories). Lat-A stands for Latrunculin-A and BFA for Brefeldin-A.
As briefly mentioned in the caption of Supplementary Fig. 15b, if confinement would be effectively present and related to compartmentalization of the cytoplasm, treatments with drugs that affect the cytoplasm organization should induce a significant decrease of the fraction of confined QDs and/or an increase in the mean box size. Nevertheless, any change at all was found for cells treated with Nocodazole, a microtubule-depolymerizing drug. Treatment with Latruculin-A or Brefeldin-A, which respectively disrupts the actin cytoskeleton and the Golgi apparatus, inversely to expectations, caused a slight decrease of the box size and a mild increase of the fraction of confined trajectories. Moreover, analysis of simulated trajectories showed that a large fraction (60%) of time-averaged MSDs of freely diffusing trajectories, with similar characteristics as those observed for QDs data (see Methods for details), could be as well fitted with a confined diffusion model, as a consequence of the intrinsic variability of Brownian motion and MSD curves, resulting in a mean box size of 850 nm.
Altogether, this suggests that the putative confinement found for QDs principally reflects the limited extent of the temporal window of observation of their dynamics and not real confined diffusion.

Supplementary Table 3

NPs	Zeta potential (mV)	Immobile fraction (%)	D_{60ms} ($\mu m^2 \cdot s^{-1}$)	
QDs-PEG-NH_2	-6.5	36 ± 15	0.15	
QDs-streptavidin	-15	24 ± 6	0.16	
QDs-COOH-PEG	-10.5	13 ± 4	0.09	
QDs-peptide	-	46 ± 22	0.04	
QDs-Itk-COOH	-41.7	49 ± 19	0.025	
25nm Rho-NPs	-14.5	5 ± 3	D_{slow} 0.5	D_{fast} 1.34

Supplementary Table 3 | Properties and diffusivity of NPs of about 25nm-size

The diffusivity parameters (immobile fraction and D_{60ms} values) reported in the Table refer to NPs internalized in (untreated) HeLa cells via pinocytosis.
NPs are assumed to be immobile if their MSD curve is smaller than the pointing accuracy of our imaging systems (~60 nm). Errors on the immobile fraction are SEM.
The number of trajectories used for the calculation of the diffusivity parameters are: $N = 1696$ for QDs-PEG-NH_2, $N = 685$ for QDs-streptavidin, $N = 6531$ for QDs-COOH-PEG, $N = 785$ for QDs-peptide, $N = 915$ for QDs-Itk-COOH, and $N = 1314$ for 25nm Rho-NPs.